4.4
SHORT-TIME FLUCTUATIONS OF THE CONVECTIVE BOUNDARY LAYER HEIGHT AND ENTRAINMENT PROCESSES OBSERVED WITH DOPPLER LIDAR

K. Träumner[1], A. Wieser, C. Kottmeier and U. Corsmeier
Institut für Meteorologie und Klimaforschung
Karlsruhe Institute of Technology, Karlsruhe, Germany

Small-scale fluctuations of the convective atmospheric boundary layer (CBL) are investigated using a $2~\mu m$ Doppler lidar. It is shown that the CBL height does not respond directly to the current vertical wind underneath. Instead CBL height at a fixed location reflects the processes the air mass experienced upstream. Different statistically based concepts of an entrainment zone and the definition as a transition zone using aerosol backscatter are analyzed and compared. Relationships between entrainment zone thickness, entrainment velocity and Richardson number, as a measure of stability, are examined and applied to relations from laboratory experiments and Large Eddy Simulation (LES). Several event-like processes can be identified from visualized Lidar data as relevant for entrainment.

1 Introduction

Observations of the daytime planetary boundary layer height (BLH, z_i) show many fine-scale structures at spatial scales of a few ten meters and time scales of minutes at a fixed location (e.g. Flamant et al., 1997; Haegeli et al., 2000). Although the importance of these variations for the downward flux of warmer and dryer air from the free atmosphere into the boundary layer (BL) is generally accepted, detailed research on them is quite rare. The diurnal CBL growth is driven by this entrainment process but is simultaneously influenced by many other factors (e.g. turbulence, surface fluxes or vertical wind; Turner, 1986).

This study is based on data from a $2~\mu m$ Doppler lidar and radiosondes. In contrast to previous studies, it includes the high resolution vertical wind data in the BL. Lidar backscatter and the line-of-sight velocity information is used to determine BLH. Different concepts describing the entrainment zone (EZ) are compared and related to results from former studies using measurements in the atmosphere and from laboratory experiments. The relationship between the short-time fluctuations and the underlying wind field is investigated. Using smoothing and interpolation techniques it is possible to visualize several entrainment processes, which are presented in section 8. Finally the diurnal development of the observed BLH was used to calculate entrainment velocities. This study comprehends itself as an attempt bringing the knowledge from the laboratory and simulation into the real atmosphere.

2 Overview on entrainment

Entrainment, as we understand, describes the process of transporting air from a stable stratified layer above

into a turbulent layer. It was subject of research in laboratory experiments (Linden, 1973; Deardorff et al., 1980; Mc Grath et al., 1997) and Large Eddy Simulations (LES) (Carruthers and Moeng, 1987; Sullivan et al., 1998). In the atmospheric boundary layer the EZ is defined as the upper part connecting the mixed layer to the free atmosphere. The EZ is thermodynamically stable and reaches typically 25% of the BLH (Deardorff et al., 1980). Measurements of entrainment and entrainment zone thickness (EZT, Δh) in the atmosphere (e.g. Boers and Eloranta, 1986; Davis et al., 1997) are difficult, due to the need of high temporal and vertical resolution measurements of the atmospheric boundary layer over several hours.

The entrainment velocity is defined

$$w_e = \frac{dz_i}{dt} - w_L \qquad (1)$$

with w_L is the large scale lifting or sinking of the air mass.

Entrainment processes were studied in tank experiments. Four different mechanism were distinguished (Carruthers and Moeng, 1987): (i) a large scale engulfment, incorporating large volumes of the non turbulent fluid mechanically into the adjacent turbulent environment (Screenivas and Prasad, 2000), (ii) breaking Kelvin-Helmholtz instabilities, (iii) entrainment by small fluid filaments due to BLH deformation by large eddies (Linden, 1973) and (iv) breaking of internal waves (Fernando and Hunt, 1997). The Richardson number Ri at the interface controls which process dominates. It is defined as

$$Ri = gz_i \frac{\Delta\rho}{\rho} \frac{1}{u^2} = \frac{g\Delta\theta}{\theta_V} \frac{z_i}{u^2} \qquad (2)$$

with mean air density of the CBL ρ, density jump at the interface $\Delta\rho$, respectively the potential virtual temperature θ_V and $\Delta\theta$, and a characteristic velocity scale u. In this study a combined velocity scale from Tennekes

[1]Corresponding author address: Katja Träumner, Institut für Meteorologie und Klimaforschung, Forschungszentrum Karlsruhe, Hermann-Von-Helmholtz-Platz 1, 76344 Eggenstein-Leopoldshafen, Germany; email: katja.traeumner@imk.fzk.de

and Driedonks (1981) $u^2 = w_*^2 + 4u_*^2$, using the convective velocity scale $w_* = \left(\frac{gz_i}{\theta_V} \cdot (\overline{w'\theta'_V})_s \right)^{\frac{1}{3}}$ and additionally the friction velocity $u_*^2 = (\overline{u'w'} \mid_s^2 + \overline{v'w'} \mid_s^2)^{0.5}$, was used as velocity scale. In the cases of fully convective conditions $u \simeq w*$ was valid.

Sullivan et al. (1998) visualized entrainment processes using LES. They observed large scale engulfment at small Ri (Ri=13.5) and a pull-down of pockets of warmer air near plume's edges at large Ri (Ri=35). Wave breaking could not be observed by them. Mc Grath et al. (1997) measured in laboratory experiments that with increasing Ri first the impinging of eddies, then the shearing of interfacial-layer fluid by eddies and finally the breaking of interfacial waves became the dominant mechanisms.

Models and experiment results assume, that both, the entrainment velocity

$$\frac{w_e}{U} = f(Ri) \qquad (3)$$

and the EZT

$$\frac{\Delta h}{z_i} = f(Ri) \qquad (4)$$

are functions of Ri. The well known and often used relations $\frac{w_e}{w_*} = 0.25Ri^{-1}$ and $\frac{\Delta h}{h0} = 0.21 + 1.31Ri^{-1}$ with $h0$ is the lower boundary of the EZ, were obtained by Deardorff et al. (1980) under convective conditions. Other studies showed slightly varying exponents (Turner, 1986; Batchvarova et al., 1997).

3 Data sets

To check the applicability of the high resolution BLH algorithms, two data sets have been used: the Convective Storm Initiation Project (CSIP) conduced in summer 2005 in Southern England (Browning et al., 2007) and the Convective and Orographically-induced Precipitation Study (COPS) from summer 2007 in Southwest Germany (Wulfmeyer et al., 2008). The major difference concerning the lidar measurements is the terrain complexity. The CSIP site is gently rolling terrain, whereas COPS was performed in a mountain region, where the lidar was operated on the top of Hornisgrinde mountain (1160 m asl).

This study focused on clear air days and days with light cumulus convection. Due to a need of lidar vertical stare measurements, totally 4 days during CSIP and 4 days during COPS were favorable and evaluated.

The Doppler lidar is a Lockheed Martin Coherent Technologies $2\ \mu$m Windtracer. It provides a pulse repetition frequency of 500 Hz and a pulse providing a spatial resolution of approximately $72\ m$. An effective data rate of wind data of 1 Hz was achieved by averaging over 500 pulses. An energy balance station was located close to the Doppler lidar during both campaigns, and delivered latent and sensible heat fluxes at the surface and wind at 4 m agl. Radiosondes of type Graw

DFM97 were launched from the measurement site at least every 2 hours during intensive observation periods (IOPs) on all CSIP days . During COPS, radiosondes of type Vaisala RS92 were launched every 3 hours on 3 of the 4 days from the measurement site at Hornisgrinde mountain and from a site in the Rhine Valley at 140 m asl at 9.8 km distance from the lidar location.

Small-scale fluctuations of the CBL at time scales of several minutes were analyzed using CSIP data only.

4 Boundary layer height determination

The common method for convective BLH determination using lidar is the localization of the interface between the mixed layer with high aerosol content and a quasi aerosol free atmosphere above. Four different automatic methods based on the range-corrected backscatter profile were implemented to determine the CBL: (i) a threshold technique using the mean backscatter value between mixed layer and free atmosphere (e.g. Batchvarova et al., 1997), (ii) by calculating the minimum derivative (e.g. Flamant et al., 1997), (iii) by fitting an idealized backscatter profile to the measured profile (Steyn et al., 1999) and (iv) by using a wavelet analysis (e.g. Cohn and Angevine, 2000). To stabilize the algorithms a set of preoperations were applied to each profile: data with too low SNR was neglected and profiles were averaged over 10 seconds. Using a threshold value for cloud backscatter, clouds were located and CBL-clouds were distinguished from decoupled clouds. If a CBL-cloud was detected, the cloud base was used to estimate BLH. Unrealistic high BLHs ($> 3000m$) as well as temporal jumps of BLHs of over 200 m were neglected. A subjective inspection was used to find accumulations of detected BLHs at a second altitude e.g. due to additional layers. A point-to-point assortment was not performed. Fig. 1 gives an example for the BLH determination using the four methods.

The idealized-profile method seemed to deliver best temporally consistent results in particular because of using the hole profile instead of only several data points. If any of the other methods also detected the BLH in the range of $\pm 100\ m$ around the result of the idealized-profile method, the idealized-profile value was taken as the lidar aerosol BLH.

The wind information from Doppler lidar could be used to determine BLH as well. Using the definition of the mixed layer as the layer of high turbulence (Stull, 1988) the profile of the vertical velocity variance (σ_w) was used to detect BLH (Fig. 2). For that purpose an idealized variance profile based on a profile given by Lenschow et al. (1980)

$$\frac{\sigma_w^2}{w_*^2} = 1.8 \left(\frac{z}{z_i} \right)^{\frac{2}{3}} \cdot \left(1 - 0.8\frac{z}{z_i} \right)^2 \qquad (5)$$

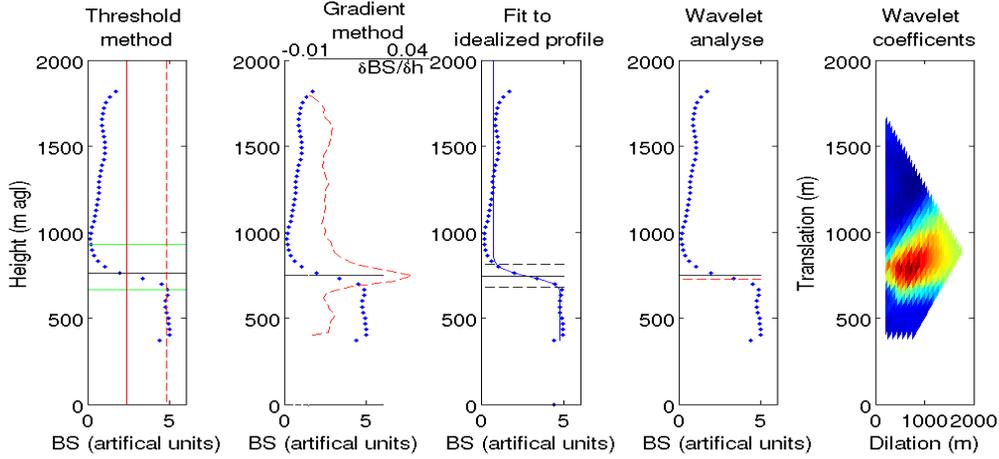but with an adaption to the shape of the measured pro-

Figure 1: BLH by automated algorithms (from left to right): threshold value, minimum derivation, idealized profile and wavelet analysis, BS lidar backscatter signal
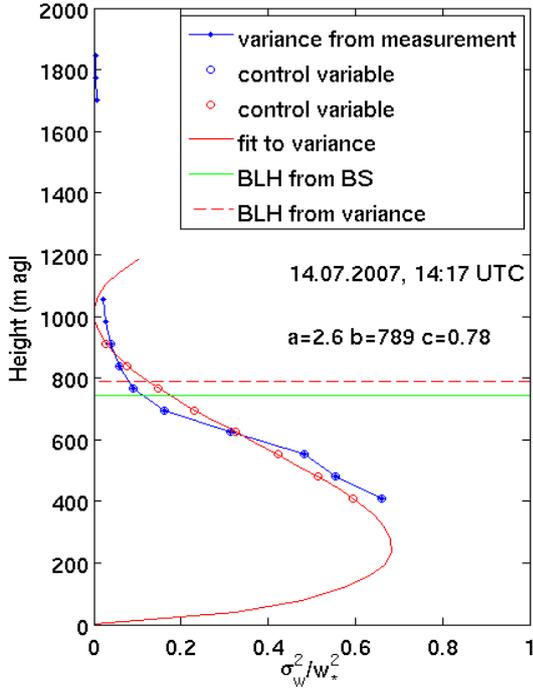

Figure 2: BLH from vertical velocity variance. An idealized profile is fitted to the measured data.

file

$$\sigma^2_{w_{fit}}(z, a, b, z_i) = \left(\frac{g \cdot \overline{w'\theta'}_s}{\theta} \right)^{2/3} \cdot a \cdot z^{\frac{2}{3}} \cdot \left(1 - b\frac{z}{z_i} \right)^2$$

(6)

was fitted to 60 minutes variance profiles. In this study the turbulent heat flux at the surface $\overline{w'\theta'}_s$ was measured by energy balance station and could be used as an input. It would be also possible to disregarded $\overline{w'\theta'}_s$ due to the fit parameter a. A large difference between the measured profile and the fit, due to either non-existing turbulence or to deviant shape, led us to neglecting the BLH estimated from this method.

Furthermore an independent BLH was estimated from radiosonde potential temperature profile using the method of Driedonks (1982).

5 Aerosol layer height and turbulence

The diurnal cycle of the BLH was determined by applying smoothing cubic splines to hourly averaged values. The results using the aerosol profiles and the turbulence profiles are shown in Fig. 3 and Fig. 4. The 4 CSIP cases showed typical daily evolutions, with growing mixed layer up to the afternoon, followed by a short period of stagnant height. The maximum height was reached at different times ranging from 14 to 17 UTC. For the COPS cases the aerosol heights showed on two of the four days a different evolution, with decreasing BLH levels until afternoon (Fig. 4). Three of the four cases show the expected diurnal variations using BLH from turbulence profiles. The exceptional day was the 15 July, 2007, when a synoptic frontal passage happened. In comparison to the CSIP cases, turbulence appeared later over the mountain site and the BLH reached lower heights over ground, but similar heights over sea level.

For CSIP 28% of the averaged aerosol BLHs were not connected to turbulence BLHs, 49% for COPS respectively, if only the time period between 8 to 20 UTC was taken into account. Together with Fig. 3 and 4 a problem in determining BLH from aerosol backscatter profiles is observable: Aerosol layers, resulting from advection or venting processes, might be wrongly identified as CBL. This is apparent especially over complex terrain (de Wekker et al., 2004). Nevertheless 68% (CSIP) respectively 77% (COPS) of simultaneously determined BLH from aerosol and from vertical velocity variance matched within 150 m.

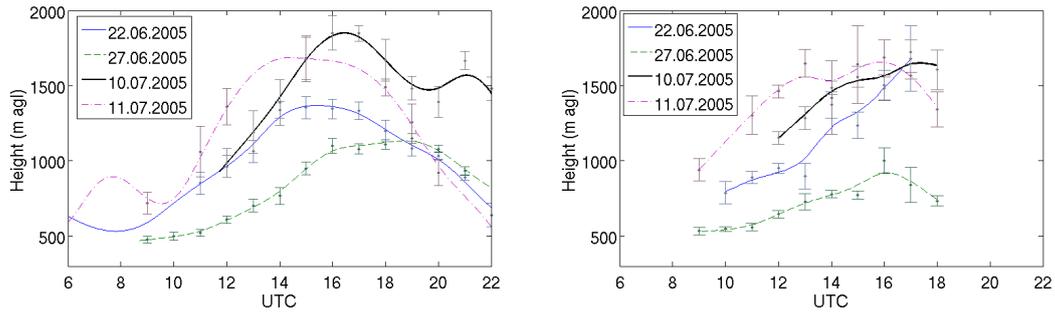A comparison to BLH from radiosonde data is shown

Figure 3: Diurnal cycle of the BLH determined from aerosol (left) and from turbulence (right) for 4 CSIP cases
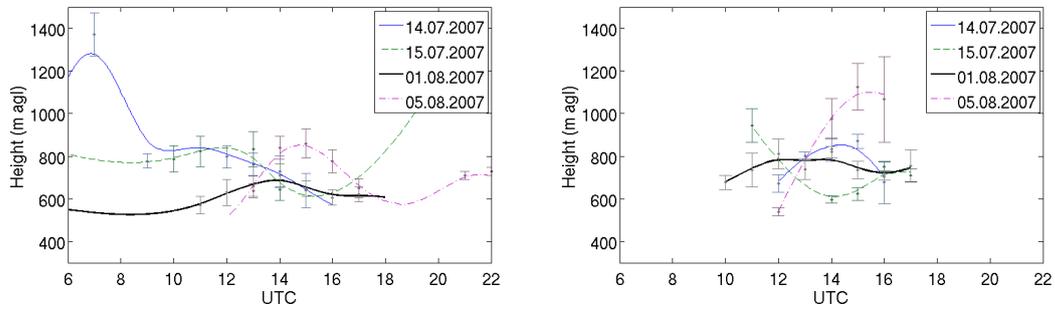

Figure 4: Diurnal cycle of the BLH determined from aerosol (left) and from turbulence (right) during 4 COPS cases
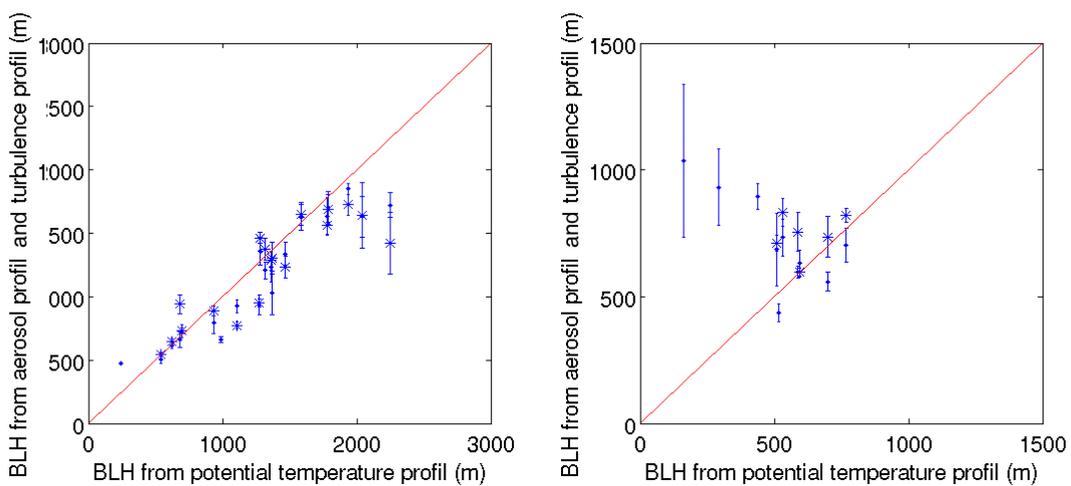

Figure 5: Comparison of lidar BLH from aerosol profiles (dots) and turbulence profiles (stars) with BLH from radiosondes, CSIP left, COPS right. The errorbars indicate the standard deviations of the BLH ± 15 minutes around radiosonde ascent for aerosol data, respectively a fluctuation range in the associated hour for turbulence data.
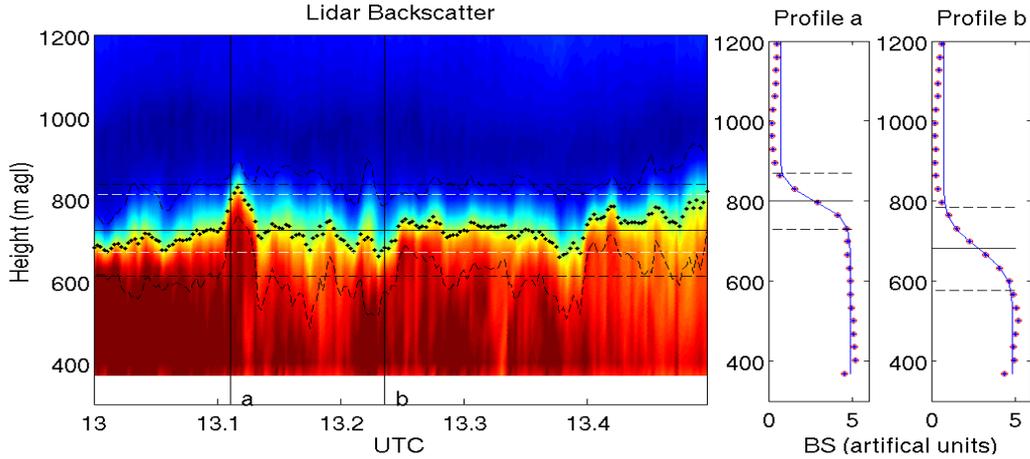
Figure 6: Variability of the transition zone for a measurement example from the 27 June, 2006: BLH (dots) and transition zone (black line, dashed) determined using the Fit-to-an-idealized-profile-method. Two examples show the variability of the backscatter profile during small time intervals (right). Also included as horizontal lines are the mean BLH (black line, solid), the 4th and the 98th percentile (horizontal white line, dashed) and the mean transition zone (horizontal black line, dashed).

in Fig. 5. The agreement between BLH from turbulence profiles and BLH from potential temperature was better during COPS and worse during CSIP. Thus a conclusion which method is more suitable was not possible.

The advantage of using aerosol profiles is an higher temporal resolution. The wrongly identification of advected or vented aerosol layers as CBL is a drawback. The turbulence profile method provided a possibility to detect the turbulent boundary layer and to exclude errors due to high aerosol levels in the morning from the previous day (residual layer) or night (advection). As well it allows to identify the transition from turbulent to residual layer in the evening. But due to the need of a sufficient amount of data to get statistically stable results, the time resolution of the BLH from turbulence profile is too low to identify small-scale fluctuations. Thus the turbulent layer height is used as a control parameter for the consistence of the aerosol heights with turbulent mixture for further analysis.

6 Concepts of entrainment zone thickness

Basically two approaches for EZT are common: estimation from BLH variability (e.g. Flamant et al., 1997) or from the transition zone of a profile, e.g. aerosol profile (Haegeli et al., 2000). The first approach is a statistical method and needs a sufficient amount of data, the second method can be applied to each measured profile. The BLH variability is estimated here from the standard deviation (σ_{z_i}) and from a percentile analysis using one hour data intervals, containing data at least during 60% of time. The BLHs were detrended to exclude the effects of daily BLH evolution. The four CSIP cases were analyzed from 8 to 20 UTC with time steps of 10 minutes. Following Davis et al. (1997) the 4th ($h0$) and the 98th percentile ($h2$) was calculated

and following Cohn and Angevine (2000) the 15th and 85th percentiles. From one of the fit parameters of the idealized profile method (section 4) the transition zone was calculated. Because of the necessity of a defined transition zone, a minimum value of $30\ m$ and a upper threshold of $750\ m$ was used. Fig. 6 shows the variability of this zone from one profile to another. For intercomparison with the statistical concepts the values were averaged over 60 minutes as well.

The fluctuations of the BLH follow a symmetric distribution, which can be described as Gaussian for small differences and as a Lorentz distribution at the edges. The correlation between the two statistical ratios of the EZT to the BLH, $\frac{\sigma_{z_i}}{z_i}$ and $\frac{h2-h0}{z_i}$, was between 94% and 99% for 4th and the 98th percentile, and 91% and 98% for the 15th and 85th percentile respectively (Fig. 7) using the 4 CSIP days. This is in agreement with former results from Davis et al. (1997), who analyzed airborne measurements (red stars in Fig.7). The depth of the EZ using the standard deviation agreed roughly with the distance between the 15th and 85th percentile and half the distance between 4th and the 98th percentile.

The fit algorithm to determine transition zone failed when clouds occurred. Under heterogeneous BLH the upper limit of the transition zone was reached frequently. As a result a satisfying determination of the transition zone was only possible for two of the four days. On these two days the correlation coefficient between the transition zone and the 4th and the 98th percentile was 62% and 80%. In 90% of time, the hourly averaged transition zone was thicker than the distance between the 4th and the 98th percentile. Fig. 8 shows an example of a diurnal cycle of the different EZT concepts. All approaches show variations during the day, but a typical diurnal cycle was not observed.

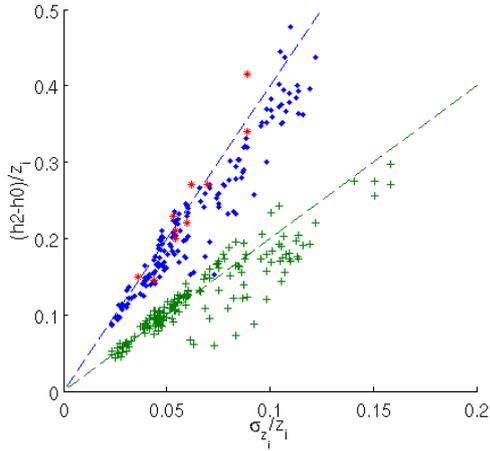The transition zone concept seems to be the most

Figure 7: Correlation between different statistical concepts for the entrainment zone: distance between the 4th and the 98th percentile (dots and stars), distance between 15th and 85th percentile (plus)
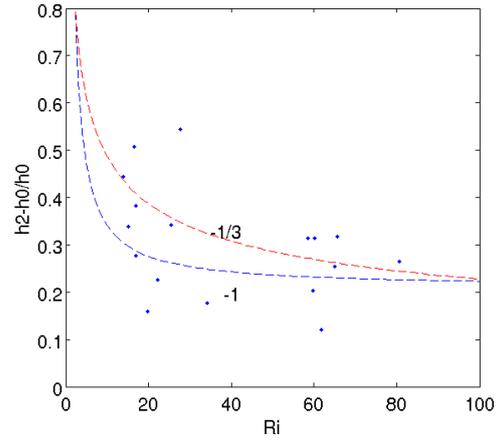

Figure 10: Relationship between Richardson number and entrainment zone. Best fit using a Ri^{-1} dependency (blue line) and a $Ri^{-1/3}$ dependency (red line)
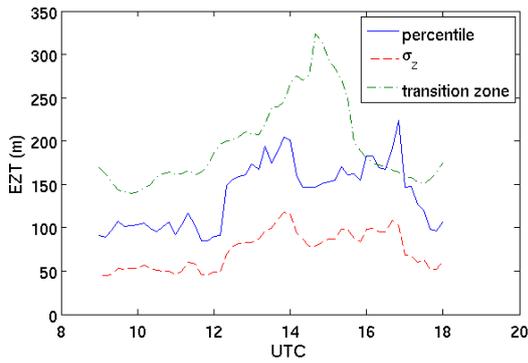

Figure 8: Diurnal cycle of EZT using different EZT concepts for 27. June, 2005.
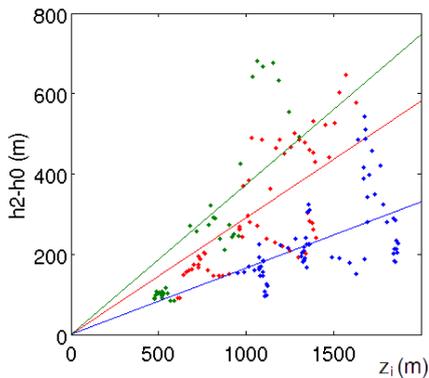

Figure 9: Relationship between EZT and BLH, during 8 to 12 UTC (green dots), 12 to 15 UTC (red dots) and 15 to 18 UTC (blue dots) and the best linear fit through the data (solid lines).

descriptive approach (Fig. 6), able to detect even short variations in the EZ. The percentile analysis was more robust, but not able to resolve fast changes. The results indicated, that mixing of entrained air did not only take place in the height range of the varying tops of the BLH, but also in lower regions of the mixed layer. Using only the fluctuations of the BLH yields to a slight underestimation of the EZT.

The observed CBL structure shows that concepts of a very small EZ (zero-order-jump-models, e.g. Ball, 1960) or of EZT being a constant fraction of BLH (e.g. vanZanten et al., 1999) are not realistic. The relation between EZT and BLH is varying, however in the geometrically specified range resulting from first-order-jump-models,

$$c = \frac{h2 - h0}{2z_i - (h2 - h0)} \qquad (7)$$

$c \in [0.1, 0.4]$ for convective conditions (Betts, 1974, Stull, 1976). A slightly decrease of c during the day was measured (Fig. 9).

In previous studies (e.g. Deardorff et al., 1980; Batchvarova and Gryning, 1994) a relationship between EZT and Richarson number Ri was described. Here Ri was calculated using radiosonde potential temperature profile and turbulence measurements at the surface of the energy balance station. Fig. 10 shows the Ri against the 4th and 98th percentile EZT average ± 30min around radiosonde launch time. For intercomparison with previous studies $h0$ was used for normalization. The relationship found by Deardorff et al. (1980) and confirmed by e.g. Boers and Eloranta (1986):

$$\frac{\Delta h}{h0} = 0.21 + 1.31 Ri^{-1} \qquad (8)$$
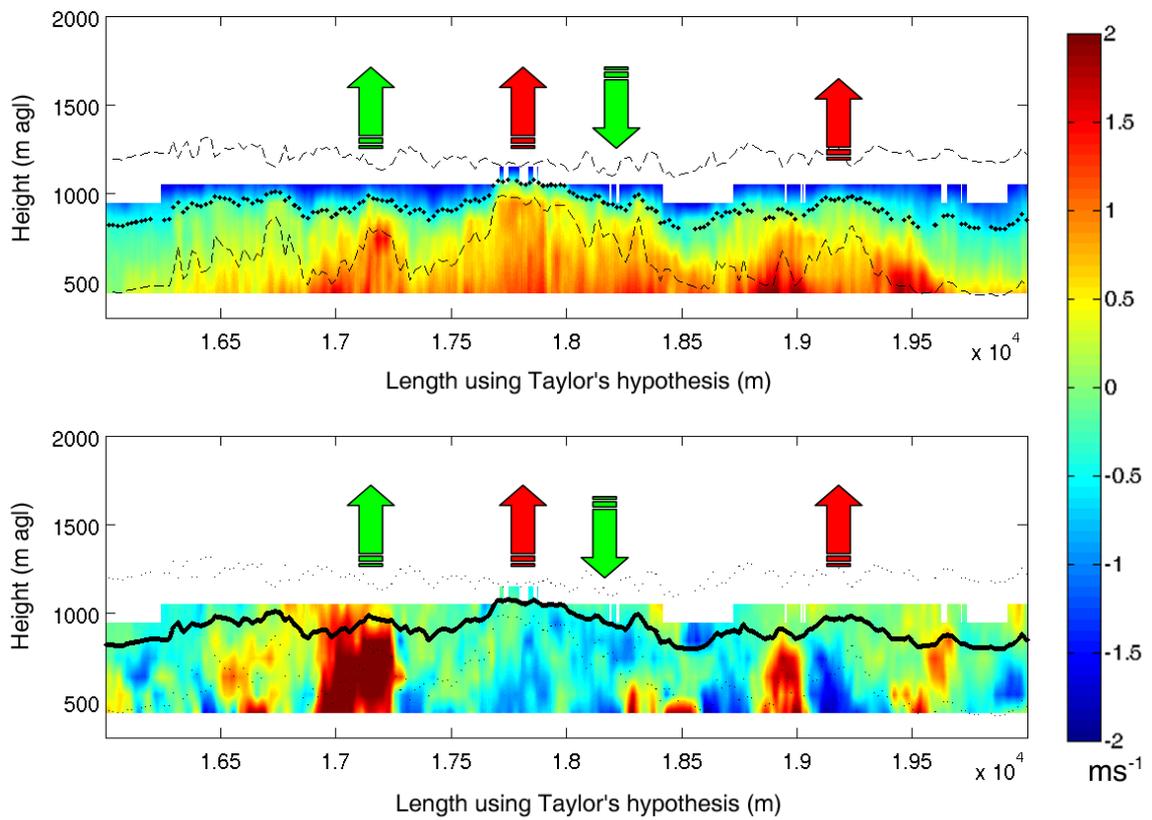
provides a good fit to the data. The best fit is

Figure 11: Short time fluctuations of the BLH and their connection to the underlying vertical windfield. The red arrows symbolice features that are anticorrelated, the green ones show correlated fluctuations.

$\frac{\Delta h}{h_0} = 1.1 Ri^{-0.34}$. A $-1/3$ law was proposed by Batchvarova and Gryning (1994). For a statistically more stable determination of the relationship data in low ($Ri < 10$) and high ($Ri > 80$) Richardson number regime is needed.

7 Correlation between short-time fluctuations and vertical wind

Short-time fluctuations of the BLH can be assumed to be connected to updrafts and downdrafts in the boundary layer. Using the Doppler lidar information this assumption was tested. Fig. 11 shows a typical 30 minutes measurement interval. Boundary layer fluctuations are partly linked to underlying updrafts or downdrafts, whereas others are uncoupled. Whether a short-time fluctuation of the BLH was directly coupled to the underlying vertical wind was not distinguishable by means of the aerosol profile.

Using Taylor's hypothesis of frozen turbulence, the measurement data was divided into 50 m intervals. For each interval the vertical velocity trend is classified using a percentile analysis of the measured vertical velocities ± 250 m around the detected BLH. Five classes are defined: strong upward, weak upward, neutral, weak downward and strong downward. Additionally a linear trend of the BLH within the intervals is calculated. A Gaussian distribution function is fitted through the absolute frequencies of the BLH trend and a classification in strong upward respectively downward (more than two times the standard deviation from the average mean), weak upward respectively downward (between one and two times the standard deviation from the average mean) and stagnant BLH was done. The results showed, that there were hardly strong downdraft regions compared to the equivalently defined updrafts. On the other hand more downdraft than updraft intervals were detected in total.

Comparing the classified vertical wind defined above and the BLH trend, the number of matches (updraft connected with upward BLH trend and vice versa) and the number of mismatches (updraft connected with downward BLH trend and vice versa) were of the same order. There was no trend of a relationship between vertical wind and BLH changes. This could be explained partly by the observation, that updrafts did not lift the boundary layer, but bulging it, an observation first described in Linden (1973). On the other hand many fluctuations and deformations were not linked to a significant wind underneath or were even in the opposite direction. For this reason the history of processes influencing the boundary layer seems to play a more important role, than the current wind field in the layer. Furthermore the CBL responds with inertial lag to plume impacts.
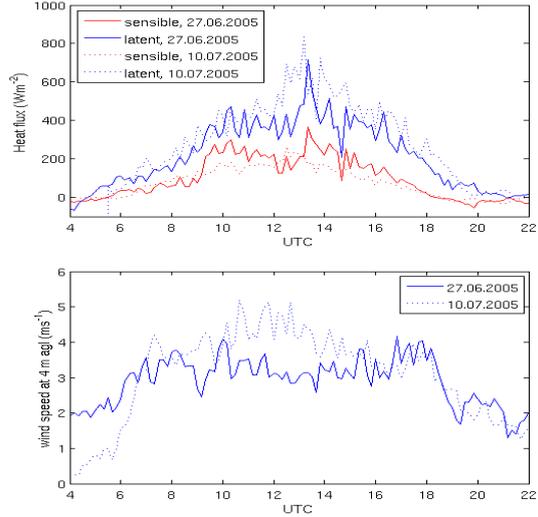

Figure 12: Latent and sensible heat flux (top) and horizontal wind velocity (bottom) for 27 June, 2005 and 10 July, 2005.

8 Visualizing entrainment processes

To visualize typical entrainment processes during specific events, the two CSIP days 27 June, 2005 and the 10 July, 2005 were evaluated. During both days mean horizontal wind velocities around 3 ms^{-1} and surface heat fluxes have been quite similar (Fig. 12). The Richardson numbers, calculated using radiosonde profiles, differ slightly (~ 25 for the 27 June, 2005 and ~ 30 for 10 July, 2005).

A 10 second averages of the lidar backscatter and line-of-sight-velocity was calculated to prevent fluctuations. A linear interpolation in horizontal as well as in vertical direction between the range gates was performed. Finally the colorbar was adapted. Using the vertical wind measurements, arrows indicating presumed motion were added in the figures.

Several processes can be identified: In Fig. 13 entrainment of filaments between and near plume structures at the 27th of June 2005, compareable to the observations of Sullivan et al. (1998) at Ri=34.5, is shown. Fig. 14 shows examples for large scale engulfment on 10 July, 2005. This enclosure of fluid was attached to smaller Ri than observed, but was not noticed on 27 June, 2005. On the 10 July, 2005 also breaking wave structures at the interface like in Fig. 15 were observed. On the 27 June, 2005 the wave structures did not break. The observed wind field suited well to the expected movement.

It could be shown, that different mechanism found in laboratory studies and LES occur in the atmosphere as well. During the two days different entrainment processes have been visualized. There was only a slight difference of the Richardson numbers, but the laboratory studies show, that switching to other processes is quite rapid.
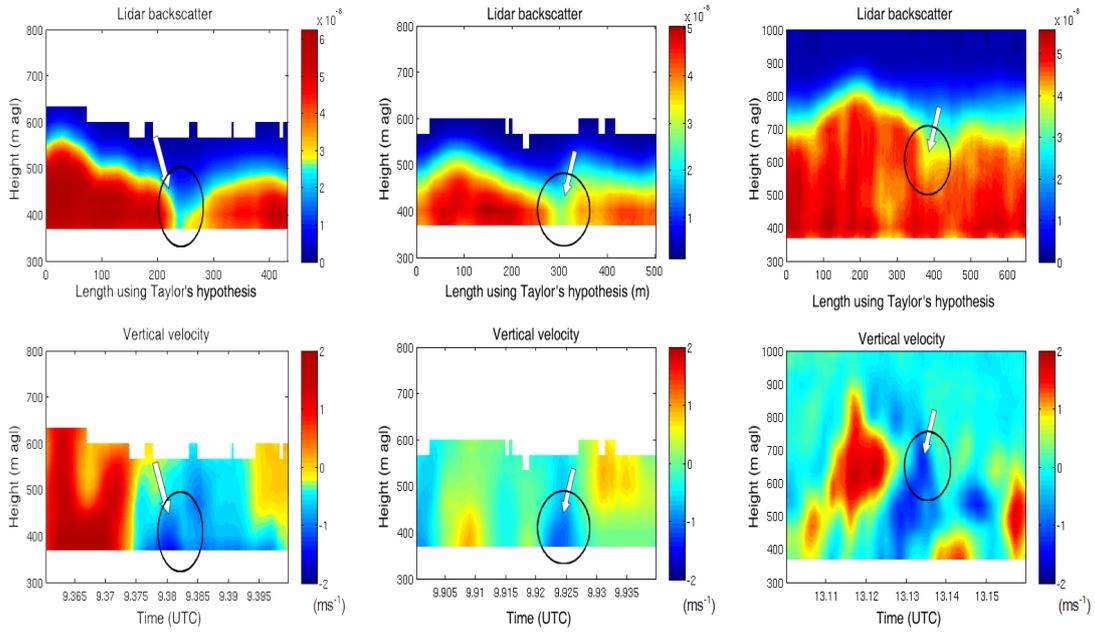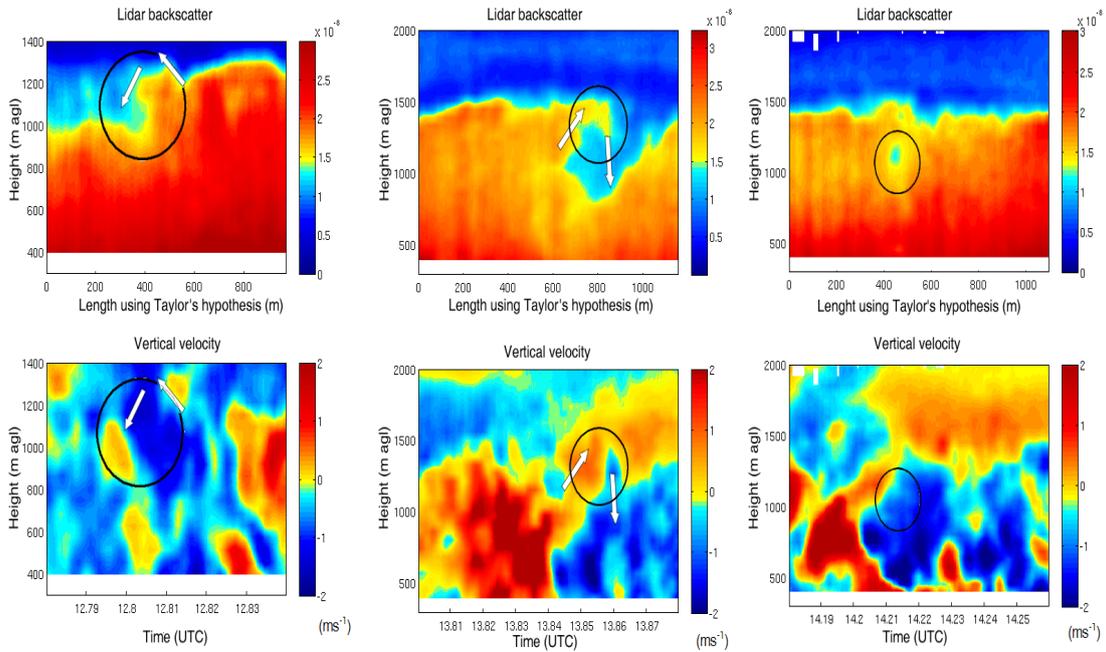
Figure 13: Entrainment at the site of large eddies

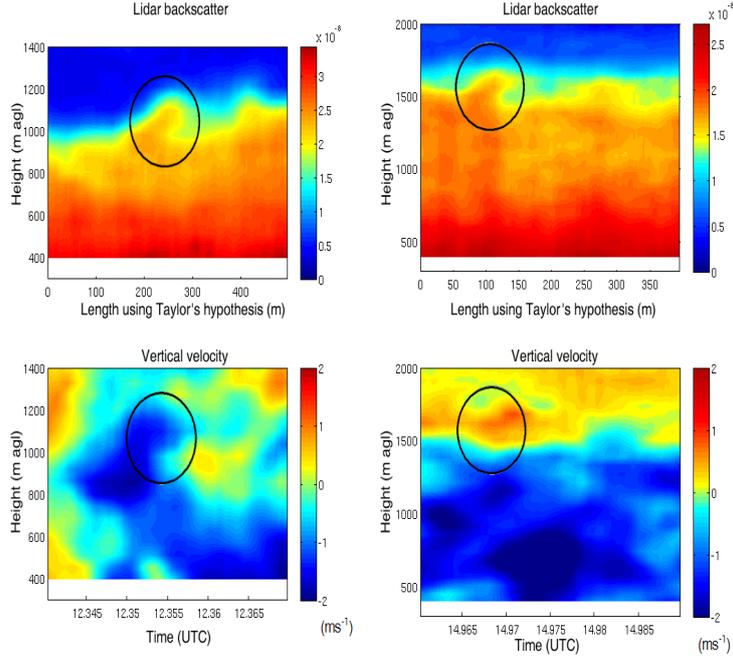Figure 14: Entrainment due to large scale engulfment.

Figure 15: Entrainment due to breaking waves

9 Entrainment velocity

Assuming that there is no large scale lifting or sinking $w_L = 0$ and no advection $\vec{v}\vec{\nabla}z_i = 0$, the entrainment velocity is calculated using smoothed daily evolutions of BLH for the four CSIP cases. To derive w_e a linear trend was fitted through 10 minutes time intervals of the smoothend BLH. Fig. 16 shows diurnal cycles of entrainment velocity. w_e is found in a range up to $8 \ cm \ s^{-1}$. On the three cloud free days (22. and 27. June, 2007 and 10. July, 2007) w_e seems to have two maxima, one in the late morning and the other in the early afternoon.

On the two days, introduced in the previous section, the maximum entrainment velocity differed by a factor of 1.7. Large scale engulfment and breaking waves seemed to be more efficient entrainment processes than the entrainment due to filaments near large eddies.

To investigate the influence of the vertical velocity, an intercomparison between the entrainment velocity and the value of the 95th percentile of the detrended vertical wind velocity was performed. A trend due to coincident higher values of the entrainment velocity to higher 95th wind percentiles was observed, but a relationship could not be identified.

Fig. 17 shows the relation between $\frac{w_e}{u}$ and Ri for all CSIP cases. About half of the data points follow a Ri^{-1} law, known from literature, but also several points with high entrainment velocities combined with large Ri occur. These points are found at all days and times. Therefore a simple explanation due to a large scale vertical motion is excluded. In spite of that a combination
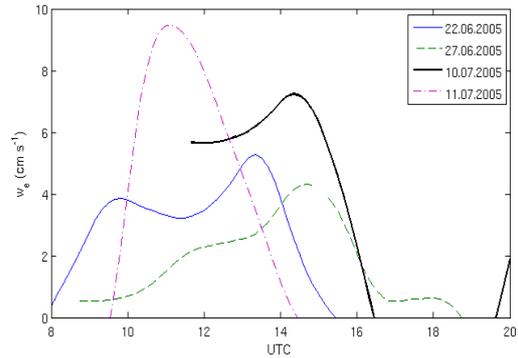

Figure 16: Diurnal development of the entrainment velocity during 4 CSIP cases.

of errors due to local Ri estimation from radiosonde, large scale and advection effects seems to be responsible. Former results from laboratory and LES could not be confirmed by the data used here.

Finally a possible relationship between $\Delta h/z_i$ and w_e/u was examined. Both are claimed to be a function of Ri. Fig. 18 shows the results for all three entrainment zone concepts. Using the relationships from Deardorff et al. (1980) there should be a linear relation between the two quantities. This is supported by the automated fit algorithm. A subjective fit through the data results in an exponent of $1/3$, taking the decreasing slope into account. This decrease is also seen in a combination of lidar data and laboratory data by Boers and Eloranta (1986). The result implies, that the entrainment velocity has a smaller dependency (smaller exponent) on Ri than the entrainment zone thickness. This appears to
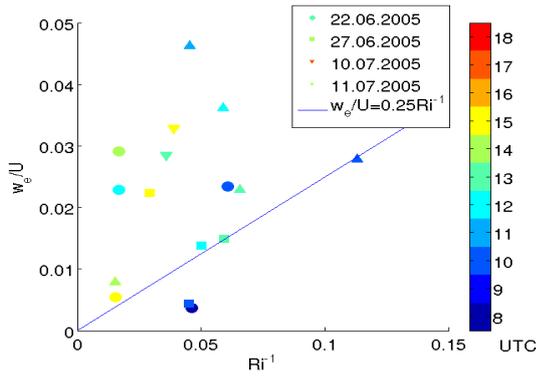
Figure 17: Correlation between Richardson number and entrainment velocity.

be contradictory to former results, where the Ri dependency of the entrainment velocity is found to be higher ($w_e/u \propto Ri^{-3/2}$ e.g. Turner, 1986) than that of the EZT ($\Delta h/z_i \propto Ri^{-1/3}$ e.g. Batchvarova and Gryning, 1994).

10 Conclusion

The aim of this study is to compare results from LES and laboratory experiments concerning entrainment to atmospheric boundary layer data. The use of a Doppler lidar enables us to get additional information about the vertical wind in the BL. BLH was determined from Doppler lidar data using different automated techniques and from radiosonde temperature profiles.

For the entrainment zone statistical concepts as well as the concept of a transition zone are examined. It can be shown, that these different approaches provide results correlated to each other. The transition zone is found to be the most realistic concept, but it is not always detectable. The fluctuations of the BLH tend to underestimate the transition zone thickness. A typical diurnal cycle of EZT is not observed. The relationship between EZT and BLH implies no direct proportionality.

Examination of the relation between the short-time boundary layer fluctuations and the underlying vertical wind showed, that the history of the boundary layer affected the variations more than the current vertical wind field associated with ascending convective plumes. Additionally the boundary layer height responds temporally lagged.

Using different smoothing and interpolation techniques, it is possible to visualize several entrainment mechanism, which lead to different entrainment velocities.

Known relationships between entrainment velocity, EZT and Ri can be affirmed only tentatively. A tendency of larger EZT having smaller Ri could be supported. The data allows dependencies of Ri^{-1} as well as $Ri^{-1/3}$. A decrease of the EZT with decreasing entrainment velocity can be shown in the convective boundary layers, with $EZT/BLH \propto w_e/u$ as clearest dependency and $EZT/BLH \propto (w_e/u)^{1/3}$ taking the few points with high ratios of EZT to BLH into account.

References

F. Ball. Control of inversion height by surface heating. *Quaterly Journal of the Royal Meteorology Society*, 86:483–494, 1960.

E. Batchvarova and S.-E. Gryning. An applied model for the height of the datime mixed layer and the entrainment zone. *Boundra-Layer-Meteorology*, 71:311–323, 1994.

E. Batchvarova, D. Steyn, X. Cai, S.-E. Gryning, and M. Baldi. Modelling the internal boundary layer in the lower fraser valley. *B.C. Proc. EURSAP Workshop on the Determination of th Mixing Height - Current Progress and Problems*, pages 141–144, Risoe, Denmark, EURSAP 1997.

A. Betts. Reply to comment on the paper 'non-precipitating cumulus convection and its parameterization'. *Quart.J.Roy.Meteor.Soc.*, 1974.

R. Boers and E. Eloranta. Lidar measurements of the atmospheric entrainment zone and the potential temperature jump across the top of the mixed layer. *Boundary Layer Meteorology*, 34:357–375, 1986.

K. Browning, A. Blyth, P. Clark, U. Corsmeier, C. Morcrette, J. Agnew, S. Ballard, D. Bamber, C. Barthlott, L. Bennett, K. Beswick, M. Bitter, K. Bozier, B. Brooks, C. Collier, F. Davies, B. Deny, M. Dixon, T. Feuerle, R. Forbes, C. Gaffard, M. Gray, R. Hankers, T. Hewison, N. Kalthoff, S. Khodayar, M. Kohler, C. Kottmeier, S. Kraut, M. Kunz, D. Ladd, H. Lean, J. Lenfant, Z. Li, J. Marsham, J. McGregor, S. Mobbs, J. Nicol, E. Norton, D. Parker, F. Perry, M. Ramatschi, H. Ricketts, N. Roberts, A. Russell, H. Schulz, E. Slack, G. Vaughan, J. Waight, R. Watson, A. Webb, D. Wareing, and A. Wieser. The convective storm initiation project. *Bulletin of the American Meteorological Society*, 2007.

D. Carruthers and C.-H. Moeng. Waves in the overlying inversion of the convective boundary layer. *Journal of the Atmsopheric Sciences*, 44(14):1801–1808, July 1987.

S. Cohn and W. Angevine. Boundary layer height and entrainment zoe thickness measured by lidars and wind-profiling radras. *Journal of Applied Meteorology*, 39:1233–1247, August 2000.

K. Davis, D. Lenschow, S. Oncley, C. Kiemle, G. Ehret, A. Giez, and J. Mann. Role of entrainment in surface-atmosphere interactions over the boreal forest. *Journal of Geophysical Research*, 1997.
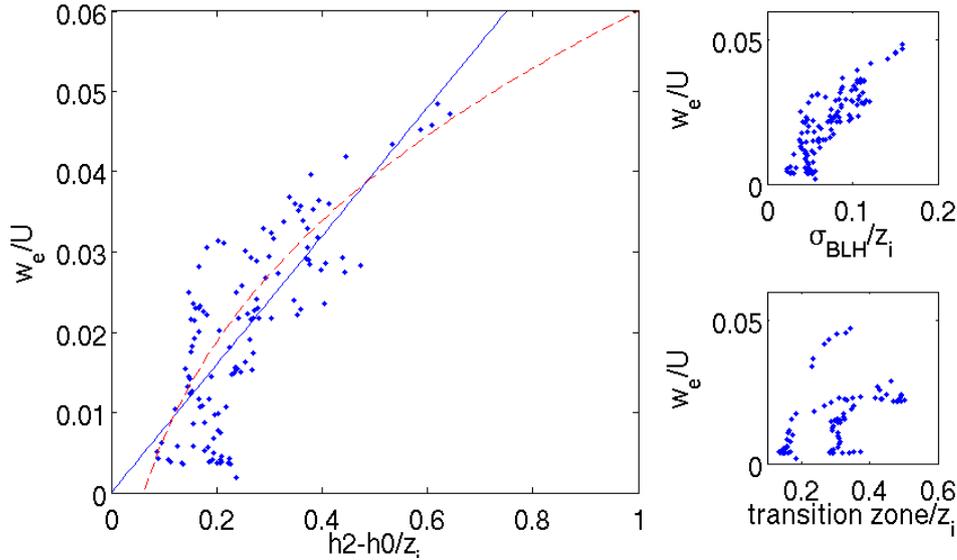
Figure 18: Correlation between entrainment zone and entrainment velocity for different EZT concepts (dots), best fit for a linear relationship (solid line) and best fit for a power 1/3 relationship (dashed line).

J. Deardorff, G. Willis, and B. Stockton. Laboratory studies of the entrainment zoneof a convectively mixed layer. *Journal of Fluid Mechanics*, 1980.

A. Driedonks. Models and observations of the growth of the atmospheric boundary layer. *Boundary Layer Meteorology*, 23:283–306, 1982.

H. Fernando and J. Hunt. Turbulence, waves and mixing at shear-free density interfaces. part 1. a theoretical model. *Journal of Fluid Mechanics*, 347:197–234, 1997.

C. Flamant, J. Pelon, P. Flamant, and P. Durand. Lidar determination of the entrainment zone thickness at the top of the unstable marine atmospheric boundary layer. *Boundary-Layer Meteorology*, 1997.

P. Haegeli, D. Steyn, and K. Strawbridge. Spatial and temporal variablility of mixed-layer depth and entrainmentzone thickness. *Boundary-Layer Meteorology*, 97:47–71, 2000.

D. Lenschow, J. Wyngaard, and W. Pennell. Mean field and second momentum budgets in a baroclinic convective boundary layer. *Journal of the Atmsopheric Sciences*, 1980.

P. Linden. The interaction of a vortex ring witha sharp density interface: a model for turbulent entrainment. *Journal of Fluid Mechanics*, 60:467–480, 1973.

J. Mc Grath, H. Fernando, and J. Hunt. Turbulence, waves and mixing at shear-free density interfaces. part 2. laboratory experiments. *J. Fluid Mech.*, 1997.

K. Screenivas and A. Prasad. Vortex-dynamics model for entrainment in jets and plumes. *Physics of Fluids*, 12(8):2101–2107, August 2000.

D. Steyn, M. Baldi, and R. Hoff. The detection of mixed layer depth and entrainment zone thickness from lidar backscatter profiles. *Journal of Atmosperic and Oceanic Technology*, 16:953–959, July 1999.

R. Stull. The energetics of entrainment across a density interface. *Journal of the atmospheric sciences*, 33: 1260–1267, 1976.

R. Stull. *An Introduction to Boundary Layer Meteorology*. Kluwer Academic Publishers, 1988.

P. Sullivan, C. Moeng, B. Stevens, D. Lenschow, and S. Mayor. Structure of the entrainemnt zone capping the convective atmospheric boundary layer. *Journal of the Atmospheric Sciences*, 55:3042–3064, October 1998.

H. Tennekes and A. Driedonks. Basic entrainment equations for the atmospheric boundary layer. *Boundary Layer Meteorology*, 20:515–531, 1981.

J. Turner. Turbulent entrainment: the development of the entrainment assumption, and its application to gepphysical flows. *Journal of Fluid Mechanics*, 173: 431.471, 1986.

M. vanZanten, P. Duynkerke, and J. Cuijpers. Entrainment parameterization in convective boundary layers. *Journal of the atmospheric Sciences*, 56(6): 813–828, March 1999.

S. D. Wekker, D. Steyn, and S. Nyeki. A comparison of aerosol-layer and convective boundary-layer structure over a mountain range during staaarte 97. *Boundary-Layer Meterology*, 113:249–271, 2004.

V. Wulfmeyer, A. Behrendt, H. Bauer, C. Kottmeier, U. Corsmeier, A. Blyth, G. Craig, U. Schumann, M. Hagen, S. Crewell, P. D. Girolamo, C. Flamant, M. Miller, A. Montani, S. Mobbs, E. Richard, M. Rotach, M. Arpagaus, H. Russchenberg, P. Schlüssel, M. König, V. Gärtner, R. Steinacker, M. Dorninger, D. Turner, T. Weckwerth, A. Hense, and C. Simmer. Research campaign: The convective and orographically induced precipitation study. *Bull. Amer. Meteor. Soc.*, 2008.